analytical chemistry

pubs.acs.org/ac Article

3D DNA Walker-Assisted CRISPR/Cas12a Trans-Cleavage for Ultrasensitive Electrochemiluminescence Detection of miRNA-141

Qian Wang,[#] Yaqi Liu,[#] Jixian Yan, Yunqing Liu, Chaomin Gao,* Shenguang Ge,* and Jinghua Yu

Cite This: *Anal. Chem.* 2021, 93, 13373−13381 Read Online

ACCESS | Metrics & More | Article Recommendations | Supporting Information

ABSTRACT: In this study, a CRISPR/Cas12a (LbCpf1)-mediated electrochemiluminescence (ECL) paper-based platform on the basis of a three-dimensional (3D) DNA walker was proposed for the ultrasensitive detection of miRNA-141. Initially, 3D-rGO with a tremendous loading space was modified on the paper working electrode (PWE) to construct an excellent conductive substrate and facilitate the growth of AuPd nanoparticles (NPs). Afterward, the AuPd NPs were introduced as the coreaction emitter medium of the 3D-rGO/PWE to provide convenience for the transformation between $S_2O_8^{2-}$ and SO_4^{2-}, amplifying the ECL emission of g-C_3N_4 nanosheets (NSs). Meanwhile, with the help of Nt.BsmAI nicking endonuclease, a 3D DNA walker signal amplifier was designed to convert and magnify the target miRNA-141 into a particular trigger sequence, which could act as activator DNA to motivate the trans-acting deoxyribonuclease activity of CRISPR/Cas12a to further achieve efficient annihilation of the ECL signal. Furthermore, the proposed multimechanism-driven biosensor exhibited excellent sensitivity and specificity, with a relatively low detection limit at 0.331 fM (S/N = 3) in the concentration range between 1 fM and 10 nM. Consequently, the designed strategy not only extended the application scope of CRISPR/Cas12a but also devoted a new approach for the clinical diagnosis of modern medicine.

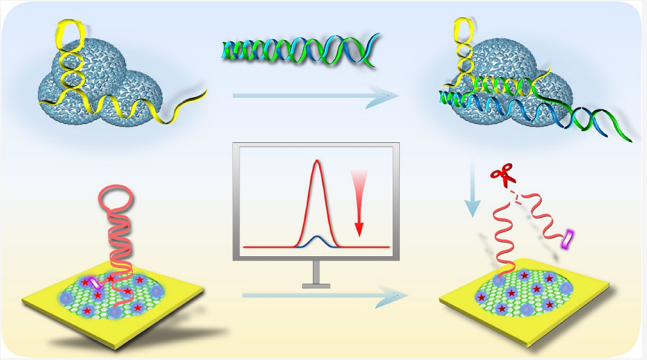

INTRODUCTION

MicroRNAs (miRNAs), as endogenous noncoding ribonucleic acids, play a decisive role in gene expression and target tracking of cancer and other tumor diseases.[1−3] As a consequence, the ultrasensitive detection of miRNAs is of great significance for the early diagnosis and biotherapy of cancer. In recent years, many universal methods, such as electrochemiluminescence (ECL),[4−6] electrochemistry,[7] fluorescence (FL),[8] and chemiluminescence (CL)[9] have been well developed to detect miRNAs. As one of the predominant techniques, ECL not only incorporates the merits of electrochemistry and chemiluminescence but also expresses a higher sensitivity, lower detection background, and wider monitoring range, which makes it outstanding in the field of immunoassay and aptasensors.

For the sake of improving the signal strength of ECL detection, some nucleic acid amplification technologies, such as rolling circle amplification (RCA),[10] loop-mediated isothermal amplification (LAMP),[11] and strand-displacement amplification (SDA),[12] have been manufactured widely. Nevertheless, as a special species of nanomachines, inspired by the biological protein motors, a DNA walker can amplify the signal by providing energy to drive the walking chain, moving along a specific track, which further improves its operability, accuracy, and flexibility.[13−15] In the process of walking, driven by the strand-displacement reaction, the DNA walker can move autonomously along the predetermined orbit through a swing arm probe and track probe, improving the local concentration and achieving the accumulation of signal.[16,17] Furthermore, compared with one-dimensional (1D)[18] and two-dimensional (2D)[19] orbital DNA nanomachines, the three-dimensional (3D) orbital DNA walker[20−22] exhibits satisfactory achievements in the field of nucleic acid amplification with high-throughput cargo loading capacity, high-density walking steps, and faster target recovery rates. Therefore, through the justifiable design of the orbit, the accurate identification and multicycle amplification[23,24] of target miRNA can be realized, and the intensity of ECL signal response can be improved vigorously.

Recently, a clustered regularly interspaced short palindromic repeats (CRISPR)-Cas system with precise targeted cutting features has been explored to develop the biosensor strategy.[25−27] Among the CRISPR-Cas family, CRISPR/Cas12a (LbCpf1) protein[28−30] equipped with the function of flanking splicing characteristics is considered as a principal

Received: July 28, 2021
Accepted: September 16, 2021
Published: September 23, 2021

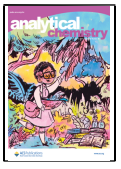

https://doi.org/10.1021/acs.analchem.1c03183
Anal. Chem. 2021, 93, 13373−13381

Scheme 1. (A) Target Conversion Principle of 3D DNA Walking Nanomachine; (B) Schematic Illustration of the Trans-Activity/CRISPR/Cas12a-Mediated ECL Biosensor for the Detection of miRNA-141

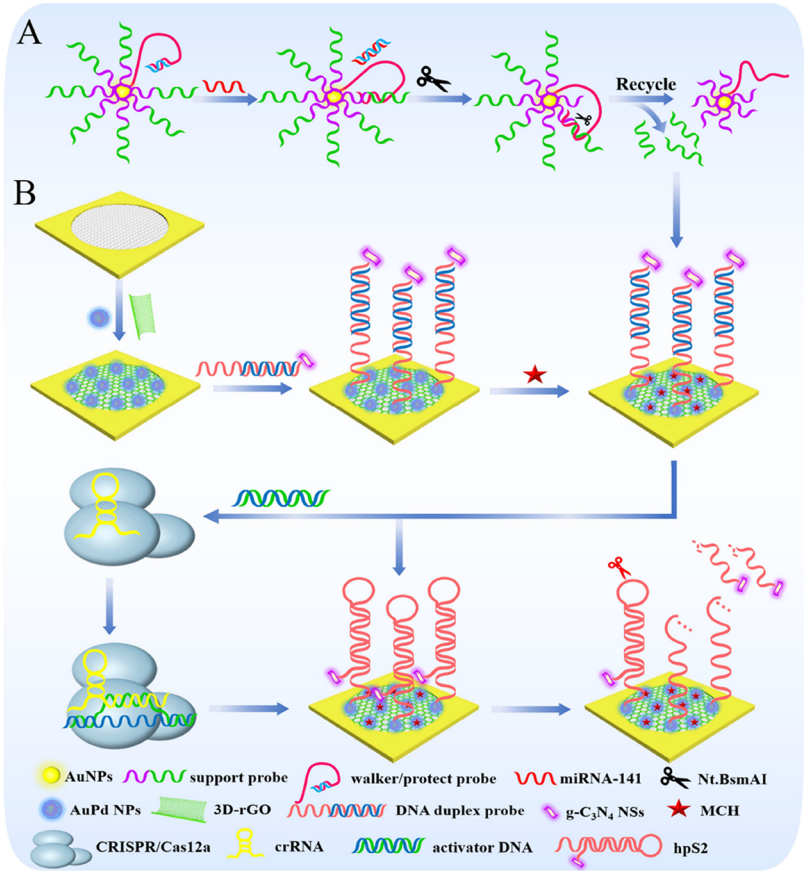

molecule of nucleotide-directed and site single-strand DNA (ssDNA) break. It has been already demonstrated to not only digest target double-strand DNA (dsDNA) (named cis-cleavage)[31] but also digest any nontarget-ssDNA without discrimination (named trans-cleavage), which leads to the superpotent lateral branch cleavage efficiency (at least 10^3 turnovers per second). In a typical splitting decomposition procedure, it can swiftly recognize the protospacer adjacent motif (PAM)[32,33] rich in T nucleotides and catalyze the maturation of the CRISPR RNA (crRNA)[34,35] to connect with activator DNA (acDNA),[36] stimulating the trans-cleavage activity[37] of the effector CRISPR/Cas12a protein to digest adjacent nontarget-ssDNA reporters indiscriminately. When dsDNA is present in biological components as a substrate with a reporter system, the side branch cleavage effect of CRISPR/Cas12a will directly transduct the ECL signal output, so as to achieve the goal of signal conversion. The lab-on-paper device (LPD)[38,39] has attracted extensive attention in the construction of biosensors because of the ultracheap cost, double-sided machinability, natural wicking characteristics, and real-time visual detection. Therefore, the nonspecific degradation technology of labeled nucleic acids to detect the existence of specific target possesses great advantages in the application of the ECL biosensor platform.

In this study, collaborated with the 3D DNA walker cascade amplification mechanism, a CRISPR/Cas12a-mediated ECL paper-based platform was proposed for the ultrasensitive detection of miRNA-141. The corresponding detailed measurement of the LPD (Figure S1) and the complete nucleic acid sequences (Table S1) are given in the Supporting Information. As shown in Scheme 1A, Au nanoparticles (NPs) with the advantage of superconductivity were utilized to anchor both the support probe and walker probe through Au−S bonds that could be paired with the protect probe to lock the operation of the 3D DNA nanomachine. As the target miRNA-141 existed and complementarily paired with the protect probe, the walker probe could be released to combine with the support probe to create restriction recognition sites. Subsequently, in the presence of Nt.BsmAI nicking endonuclease, the support probe could be specifically digested along the nucleotide orbital, which led to the releasing again of the walker probe and binding with the next support probe, thus motivating the 3D DNA walker and releasing a large amount of intermediate DNA. In addition, the loading of LPD is described in Scheme 1B, 3D-rGO with a large specific surface area inlaid with AuPd NPs was used as the modified paper working electrode (PWE) for subsequent incubation of nucleotide chains. Afterward, the g-C_3N_4 nanosheet (NS)-DNA duplex probe was connected to the electrode surface by Au−S bonds[40,41] with a considerable ECL signal (on state), and the remaining active sites were immediately blocked by 6-mercapto-1-hexanol (MCH). Then, with the incubation of intermediate DNA, S1 in the double stranded probe was released and paired to form a large number of acDNA with the PAM, while S2 automatically formed a hairpin structure to make g-C_3N_4 NSs close to AuPd NPs on the electrode surface so that the signal reached the maximum value. Ultimately, when the CRISPR/Cas12a/crRNA duplex was modified on

https://doi.org/10.1021/acs.analchem.1c03183
Anal. Chem. 2021, 93, 13373−13381

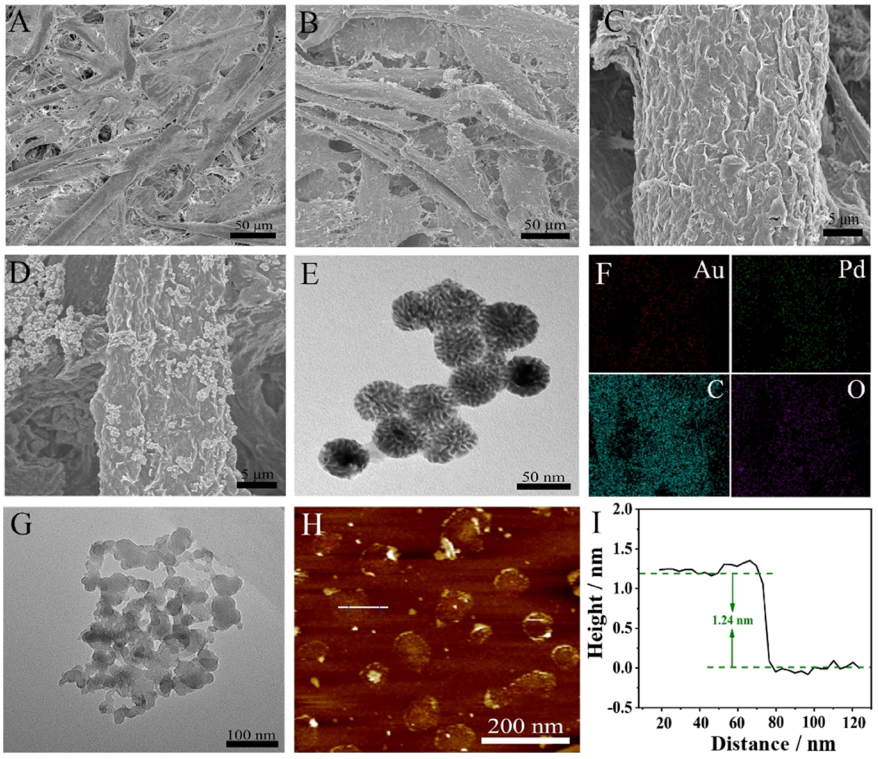

Figure 1. SEM images of (A) bare paper fibers of the PWE and (B) 3D-rGO/PWE; magnification images of (C) 3D-rGO/PWE and (D) AuPd NP/3D-rGO/PWE. TEM images of (E) AuPd NPs and (G) g-C_3N_4 NSs. The AuPd NP/3D-rGO/PWE with corresponding element mapping of (F) Au, Pd, C, and O, respectively. (H) AFM image of g-C_3N_4 NSs and (I) AFM height distribution of the observed random NSs.

the electrode, acDNA could be specifically recognized and captured, thus activating the trans-cleavage activity of Cas12a to digest all hairpin reporter S2 aimlessly to acquire the weakest signal response (off state). Therefore, using the as-proposed biosensor as a vehicle, the target miRNA could be monitored quantitatively and accurately by ECL signal response.

EXPERIMENTAL SECTION

Reagents and Instruments. The reagents and instruments are described in the Supporting Information.

Synthesis of AuPd NPs. The AuPd alloy NPs were synthesized via traditional coreduction as reported with minor modification. In a typical procedure, 400 μL of Na_2PdCl_4 (10 mM) and 41 μL of 1% $HAuCl_4$ precursor solutions were mixed quickly and dispersed with ultrasonication for 15 min. Next, 5 mL of chlorohexadecyl pyridine (HDPC) aqueous solution (10 mM), which was equipped with the ability to enhance solubility and dispersibility, was added into the above mixture. Subsequently, 0.6 mL of ascorbic acid (AA) aqueous solution (0.1 M) was added and shaken vigorously until the color changed to dark purple. The reaction system was sealed in a 35 °C water bath for 3 h to ensure the complete reduction of Au and Pd salts. Finally, the as-prepared AuPd NP gray black suspension was centrifuged (10,000 rpm, 10 min) for four or five times to eliminate the residuum and stored at 4 °C.

Preparation of g-C_3N_4 NSs and the g-C_3N_4 NS-DNA Duplex Probe. The g-C_3N_4 NSs were synthesized according to the previously reported method with a slight modification. In detail, a total of 6 g of melamine was placed into a 30 mL alumina crucible and then heated at 550 °C for 4 h with a heating rate of 2.3 °C min^{-1} in a nitrogen atmosphere, leading to yellow bulk g-C_3N_4 powder for further use. Next, a solvent desquamating method with minor adjustment was used to prepare ultrathin g-C_3N_4 NSs. Briefly, 10 mg of bulk g-C_3N_4 powder was dispersed in 10 mL of *N*,*N*-dimethylformamide (DMF) and continuous ultrasonication was performed for 18 h. Then, the final acquired dispersion solution was centrifuged at 5000 rpm for 10 min to remove the remaining undecrustated g-C_3N_4 and the supernatant was collected for following use.

The g-C_3N_4 NS-DNA duplex probe was synthesized as follows: first, 200 μL of the mixed solution including 10 μL of S1 oligonucleotide (5 μM) and 16 μL of S2 oligonucleotide (8 μM) was heated to 95 °C for 5 min by polymerase chain reaction (PCR) and gradually cooled to room temperature to gain a DNA duplex probe. Then, 50 μL of g-C_3N_4 NS supernatant was mixed in for 2 h at room temperature to acquire the g-C_3N_4 NS-DNA duplex probe conjugate.

Preparation of Intermediate DNA. The preparation and amplification of intermediate DNA was as follows. First, Au NPs were obtained by slightly improving the experimental method of traditional preparation (see the Supporting Information). In the meantime, 5 μL of walker probe (1.5 μM) and 5 μL of protect probe (1.5 μM) were mixed and annealed for 5 min at 95 °C to develop a dsDNA. Then, 100 μL of support probe (1.5 μM) and 100 μL of the above Au NP solution were introduced into the above mixture, magnetic stirring overnight at room temperature to develop the 3D DNA nanomachine. Afterward, 5 μL of the target miRNA-141 (with various concentrations) was added and automatically paired of complementary bases with the protect probe at 37 °C for 2 h, which led to the release of the walker probe. Consequently, the released walker probe could pair with the corresponding support probe, exposing the active cleavage site of Nt.BsmAI nicking endonuclease. Finally, after 5 U/mL

https://doi.org/10.1021/acs.analchem.1c03183
Anal. Chem. 2021, 93, 13373−13381

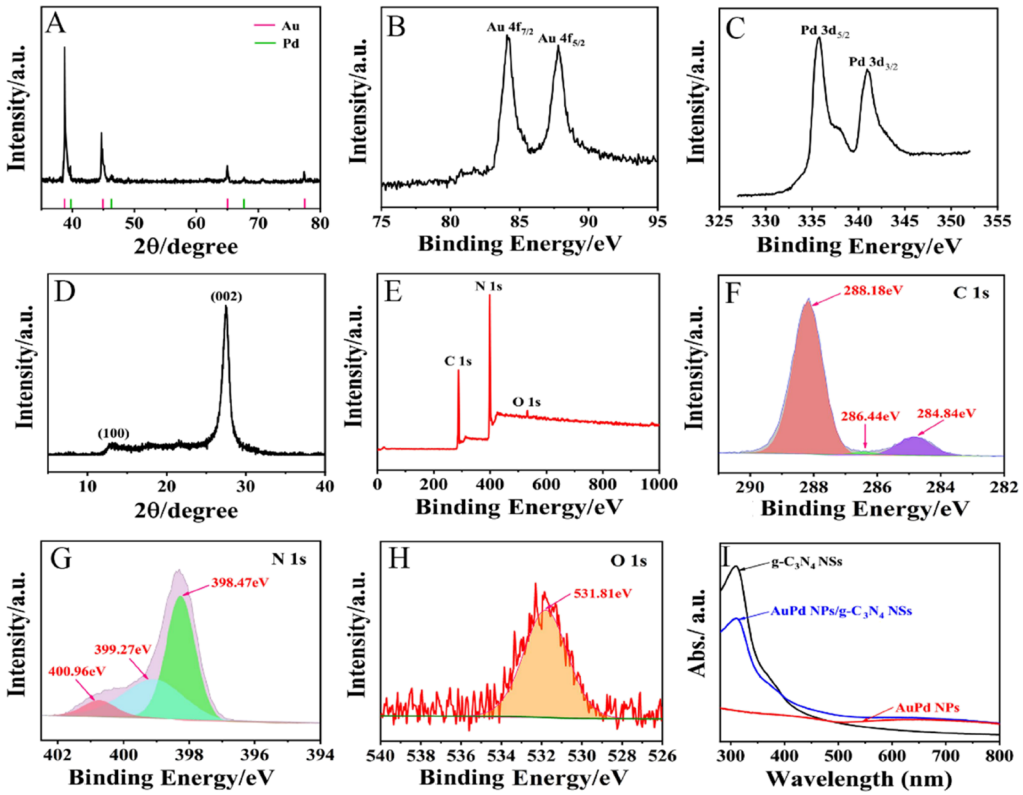

Figure 2. (A) XRD analysis, (B and C) XPS analysis of AuPd NPs. (D) XRD analysis, (E) XPS survey spectra, and high-resolution C 1s (F), N 1s (G), and O 1s (H) of the g-C_3N_4 NSs. (I) UV−vis absorption spectrum of AuPd NPs, g-C_3N_4 NSs, and AuPd NPs/g-C_3N_4 NSs.

Nt.BsmAI cutting for 2 h, a large amount of support probe fragments (called intermediate DNA) were obtained and the walker probe was released again.

Fabrication of the CRISPR/Cas12a-Mediated ECL Biosensor. Briefly, the LPD comprised three paper chip electrodes (counter electrode, working electrode, and reference electrode). First, the shape of the paper was described by the use of Adobe Illustrator (AI) software and transformed to visual paper chip (25.0 mm × 25.0 mm) by wax-printing technology (Figure S1). After being baked in an oven at 130 °C for 150 s, the printed wax melts and penetrates the paper, and the blank area (hydrophilic reaction region) (6.0 mm × 6.0 mm), three electrode area, and wax penetration region (hydrophobic reactionless region) were prepared (Figure S2). Ultimately, the as-designed fully penetrated batik paper chip was screen-printed, rinsed, and dried to remove the unfixed dyes.

Prior to modification, 20 μL of 3D-rGO dispersion was dropped by spin-coating technique and dried in the hydrophilic reaction region at room temperature, and then, the 3D-rGO-coated paper was obtained by repeated operation for three times. Next, the spherical core−shell AuPd NPs were grown in situ on the 3D-rGO-coated paper fiber substrate, which further enhanced the conductivity of the electrode. Afterward, 20 μL of the as-prepared g-C_3N_4 NS-DNA duplex probe was incubated on the modified electrode at 4 °C for 12 h. Then, the active sites on the surface of electrode were blocked with 20 μL of 1.0 mM MCH for 1 h after being rinsed with phosphate buffer saline (PBS, 10 mM, pH = 7.4). Immediately, 20 μL of the intermediate DNA, which linearly correlated with the concentration of the target miRNA-141, was incubated on the electrode at 37 °C for 2 h to pair complementary bases with S1 (from the DNA duplex probe) to form an acDNA and release S2 to form a hairpin reporter.

After this, with 20 μL of the mixture (including 100 nM Cas12a, 120 nM crRNA, 1× buffer) was incubated on the as-modified electrode at 25 °C for 1 h, and the obtained acDNA was automatically captured in which the PAM could be specifically identified by the Cas12a/crRNA complex. Then, the trans-cleavage activity toward the nonspecific stem-loop sequences in the hairpin reporter S2 was triggered in place with the combination and digestion of the Cas12a/crRNA/acDNA ternary complex. The ECL measurement was performed in 5 mL of working solution (containing 0.5 mM $K_2S_2O_8$, 10 mM PBS, pH = 7.4) with the potential from −1.3 to 0.2 V, a scan rate of 100 mV/s, and the voltage of the photomultiplier tube (PMT) at 600 V.

RESULTS AND DISCUSSION

Characterization of the AuPd NP/3D-rGO/PWE. The morphologies and structures of corresponding nanomaterials were characterized by scanning electron microscopy (SEM), transmission electron microscopy (TEM), and atomic force microscopy (AFM) technologies. As shown in Figure 1A, the coarse interface of bare paper was composed of crisscrossed fibers, which was provided with prominent flexibility and permeability. After 3D-rGO was modified, it could be observed that not only was each paper fiber tightly anchored, but also the specific surface area of the paper was magnified (Figure 1B). In the enlarged view of Figure 1C, the abundant wrinkle structure of the 3D-rGO/PWE could be witnessed more clearly, which was convenient for the improvement of conductivity and the adhesion of AuPd NPs. As illustrated in Figure 1D, the spherical AuPd NPs were firmly affixed to the

https://doi.org/10.1021/acs.analchem.1c03183
Anal. Chem. 2021, 93, 13373−13381

wrinkle crevice and the conductivity of the electrode interface was further enhanced. In order to confirm the spherical core−shell structure of AuPd NPs accurately, TEM was used for further monitoring (Figure 1E). Additionally, the equidistribution of Au, Pd, C, and O certificated the formation of the AuPd NP/3D-rGO/PWE (Figure 1F). Further evidences were contributed from the X-ray diffraction (XRD) analysis (Figure 2A) and X-ray photoelectron spectroscopy (XPS) (Figure 2B,C), demonstrating the successful preparation of AuPd NPs.

Characterization of g-C_3N_4 NSs. As for g-C_3N_4 NSs, the TEM image demonstrated that it had an irregular two-dimensional ultrathin NS structure (Figure 1G). According to the AFM image (Figure 1H), the thickness of the g-C_3N_4 NSs was about 1.2 nm (Figure 1I), which was enough to qualify for nanoluminescent material. In order to gain insights into the element composition and crystal structure, the sample was further analyzed by XRD and XPS. As shown in Figure 2D, two characteristic diffraction peaks were observed at 13.1 and 27.4° in the XRD image, corresponding to the in-plane ordering (100) of the graphitic motif and the graphitic interlayer (002) peaks, respectively. From high-resolution XPS spectra, there were only three elements (C, N, and O) discovered in the full spectrum (Figure 2E). The C 1s spectra of g-C_3N_4 NSs are displayed in Figure 2F; the peak at 288.18 eV correspond to the N−C═N coordination, and other peaks with lower intensity at 286.44 and 284.84 eV were identified as C−NH_2 and graphitic carbon (C−C) contamination, respectively. At the same time, the N 1s spectra are displayed in Figure 2G; the peaks at 400.96, 399.27, and 398.47 eV could be attributed to terminal amino functions (C−N−H), sp^3-hybridized nitrogen (N−$(C)_3$), and sp^2-hybridized nitrogen (C−N═C), respectively. The O 1s (Figure 2H) spectra exhibited a peak at 532.9 eV, corresponding to the C−O species and adsorbed water molecule. To distinguish the optical properties of materials, ultraviolet−visible diffuse reflectance spectroscopy (UV−vis DRS) was performed in the range of 300−800 nm (Figure 2I). It could be seen that the pure g-C_3N_4 NSs showed a clear peak at 330 nm, and the band gap absorption boundary was about 460 nm. After being bonded with AuPd NPs, the visible region of the absorption curve showed a bathochromic shift, confirming the optimization of g-C_3N_4 NS performance by AuPd NPs.

Characterization of CRISPR/Cas12a-Mediated Trans-Cleavage Activity. As shown in Figure 3A, in order to improve the specificity of detection, the crRNA sequence was strictly designed and the detailed information is listed in Table S1. To testify the feasibility of CRISPR/Cas12a-mediated trans-cleavage, 15% polyacrylamide gel electrophoresis (PAGE) was performed to detect the reaction of different primers, and the corresponding PAGE of the 3D DNA walker is displayed in the Supporting Information. It could be seen from the results (Figure 3B) that there was no difference between the hairpin reporter S2 (lane 1) and incubation hairpin reporter S2 with the Cas12a enzyme (lane 2). After further treatment with crRNA, a new bright band with a low molecular weight appeared (lane 3 and lane 5). Due to the large molecular weight of the support DNA/S1 duplex, strong steric hindrance would be encountered during electrophoresis, which made the migration speed of the support DNA/S1 duplex in lane 4 slower than other single-strand nucleotides. Surprisingly, the characteristic band of the hairpin reporter S2 in lane 6 vanished, demonstrating that the combination of CRISPR/Cas12a/crRNA with the support DNA/S1 duplex

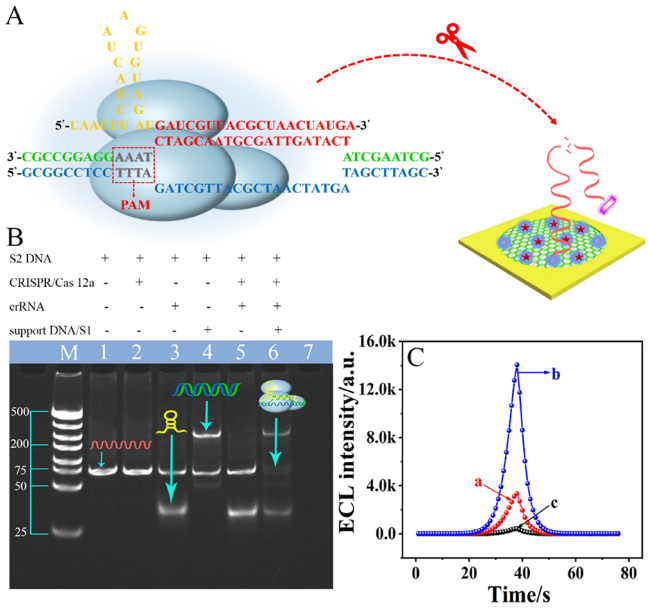

Figure 3. (A) Design of acDNA and crRNA in the CRISPR/Cas12a system for the trans-cleavage of the hairpin reporter S2. (B) PAGE analysis of hairpin reporter S2 trans-cleavage activity of CRISPR/Cas12a. M: DNA marker; lane 1: hairpin reporter S2; lane 2: hairpin reporter S2 + Cas12a; lane 3: hairpin reporter S2 + crRNA; lane 4: hairpin reporter S2 + support DNA/S1; lane 5: hairpin reporter S2 + Cas12a + crRNA; lane 6: hairpin reporter S2 + Cas12a + crRNA + support DNA/S1. (C) ECL response of the CRISPR/Cas12a-mediated biosensor under different circumstances: (a) individual g-C_3N_4 NS-modified electrode, (b) miRNA-141-incubated g-C_3N_4 NSs electrode, and (c) CRISPR/Cas12a and miRNA-141 coincubated g-C_3N_4 NSs electrode.

activated the Cas12a enzyme for nonspecific ssDNA trans-cleavage. Moreover, the trans-cleavage of the hairpin reporter by CRISPR/Cas12a was monitored by ECL response (Figure 3C). It could be found from the record that the signal of the target miRNA-141-incubated electrode (curve b) was significantly higher than that of the individual g-C_3N_4 NS-modified electrode (curve a), which was due to the formation of target-activated hairpin S2, enhancing the catalytic effect of AuPd NPs on g-C_3N_4 NSs and reaching the maximum ECL signal. As expected, only when the target miRNA-141 and the CRISPR/Cas12a/crRNA coexisted could the 3D DNA nanomachine be motivated to release specific intermediate DNA, thus activating the nonspecific trans-cleavage of CRISPR/Cas12a to the annular section, resulting in abundance of g-C_3N_4 NSs leaving the electrode surface and producing a superweak signal (curve c).

Performance and Mechanism of the Proposed ECL Biosensor. Owing to the fact that the emitter-modified g-C_3N_4 NSs exhibited powerful and steady cathode ECL activity, the influence of AuPd NPs on the luminescence intensity of g-C_3N_4 NSs was also characterized. As shown in Figure 4A, when the AuPd-modified paper was scanned toward negative potentials, the ECL response and the corresponding cyclic voltammetry (CV) curve fluctuated weakly. Apparently, in the presence of single g-C_3N_4 NSs, the ECL responded to its own signal at 6348 au with a pair of faint current redox peak, which may probably be attributed to the energetic annihilation of electrons between g-C_3N_4 NSs and $S_2O_8^{2-}$ (Figure 4B). When g-C_3N_4 NSs and AuPd NPs approached directionally on the surface of the electrode through the hairpin reporter S2, a

https://doi.org/10.1021/acs.analchem.1c03183
Anal. Chem. 2021, 93, 13373−13381

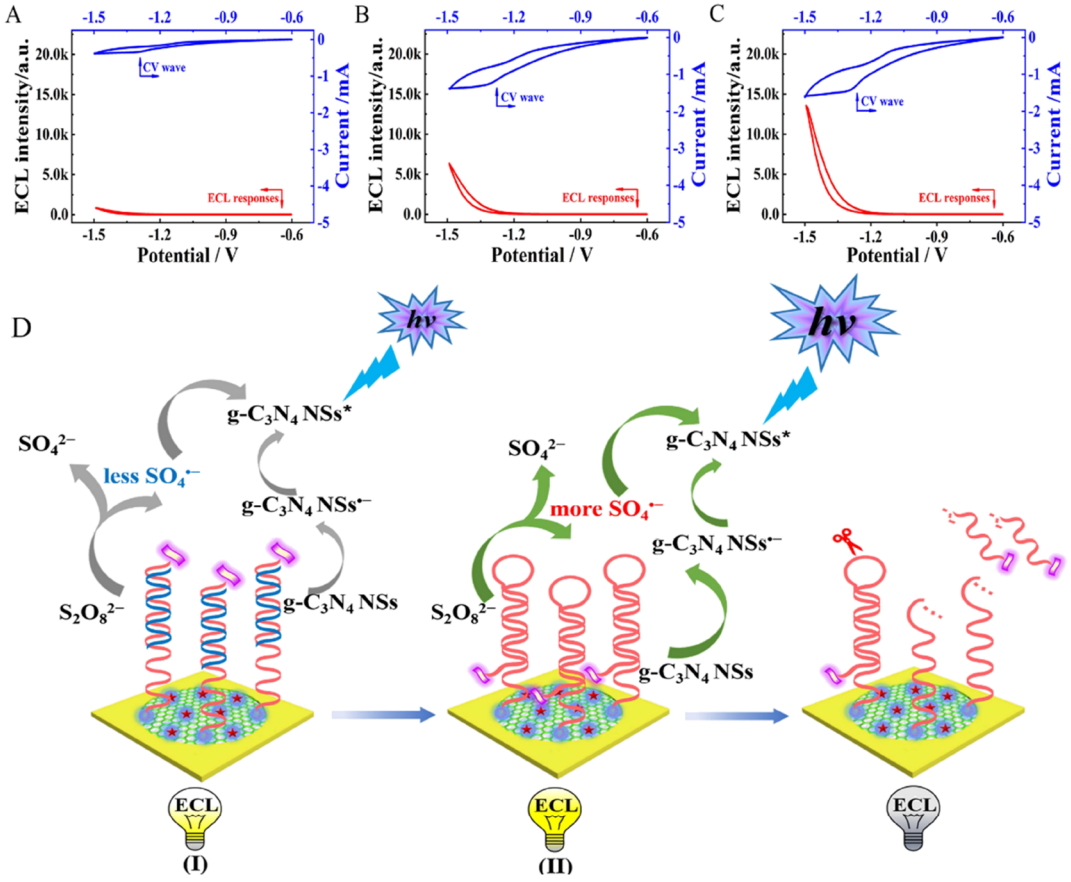

Figure 4. ECL potential profiles (red line) and the correlative peak current of CV curves (blue line) of (A) AuPd NPs (B) g-C_3N_4 NSs, and (C) AuPd NPs/g-C_3N_4 NSs. (D) ECL mechanism of g-C_3N_4 NS/$S_2O_8^{2-}$ without (I) and with (II) the acceleration of AuPd NPs.

bright ECL emission was monitored with initial and maximal potential at −0.9 and −1.29 V, respectively. The tremendous signal shown in Figure 4C could be ascribed to the quantized electricity storage property of AuPd NPs, which mediated the excessive electron injection into the conduction band of g-C_3N_4 NSs to prevent from electroreduction and accelerated the reduction of $S_2O_8^{2-}$ to produce more $SO_4^{\cdot-}$ radical hole donors. The possible detection mechanism of the ECL biosensor was revealed by the following correlated equations (corresponding amplification mechanism, see Figure 4D):

$$g - C_3N_4\ NSs + e^- \rightarrow g - C_3N_4\ NSs^{\cdot-} \quad (1)$$

$$S_2O_8^{2-} + e^- \rightarrow S_2O_8^{\cdot 2-} \quad (2)$$

$$S_2O_8^{\cdot 2-} + e^- \xrightarrow{\text{AuPd NPs}} SO_4^{2-} + SO_4^{\cdot-} \quad (3)$$

$$g - C_3N_4\ NSs^{\cdot-} + SO_4^{\cdot-} \rightarrow g - C_3N_4\ NSs^* + SO_4^{2-} \quad (4)$$

$$g - C_3N_4\ NSs^* \rightarrow g - C_3N_4\ NSs + h\nu \quad (5)$$

ECL Characterization of the ECL Biosensor. In order to investigate the modification procedures of the proposed biosensing platform, CV and electrochemical impedance spectroscopy (EIS) were implemented in an electrolyte containing 5 mM $[Fe(CN)_6]^{3-/4-}$ and 0.1 M KCl. As depicted in Figure 5A, the bare paper (curve a) exhibited a couple of distinct redox peaks. Moreover, after the immobilization of 3D-rGO, the current increased significantly, which attributed to the superconductivity of 3D-rGO (curve b). When AuPd NPs

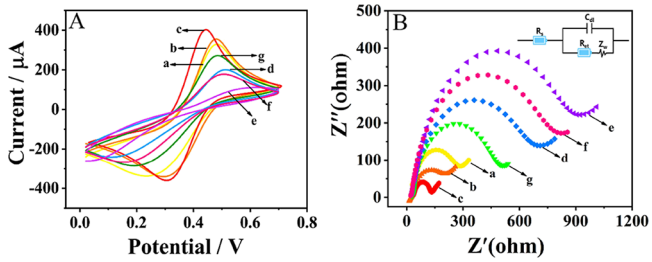

Figure 5. (A) CV curves and (B) EIS diagram with different modified procedures in 5.0 mM $[Fe(CN)_6]^{3-/4-}$ including 0.1 M KCl: (a) unmodified bare PWE, (b) 3D-rGO/PWE, (c) AuPd NP/3D-rGO/PWE, (d) g-C_3N_4 NS-DNA duplex probe/AuPd NP/3D-rGO/PWE, (e) MCH/g-C_3N_4 NS-DNA duplex probe/AuPd NP/3D-rGO/PWE, (f) intermediate DNA/MCH/g-C_3N_4 NS-DNA duplex probe/AuPd NP/3D-rGO/PWE, and (g) CRISPR/Cas12a/crRNA/intermediate DNA/MCH/g-C_3N_4 NS-DNA duplex probe/AuPd NP/3D-rGO/PWE.

(curve c) were continuously and intensively deposited on the electrode, the current response reached the maximum, which may attribute to the large specific surface area and extremely high electric conductivity of AuPd NP/3D-rGO. As electronic transfer was restricted by the mutual repulsion between the negative-charged g-C_3N_4 NS-DNA duplex probe and $[Fe(CN)_6]^{3-/4-}$, the gap of the redox peak potential showed a downward trend (curve d). While MCH was modified at the electrode interface to cover the remaining active sites, the CV curve decreased to the minimum due to the maximum electrode load (curve e). After completely incubating with the

https://doi.org/10.1021/acs.analchem.1c03183
Anal. Chem. 2021, 93, 13373−13381

intermediate DNA, S1 was specifically recognized to pair up to construct acDNA and left the electrode surface, which led to the improvement in electrical conductivity (curve f). Ultimately, not only did the arrival of CRISPR/Cas12a/crRNA absorb the acDNA to motivate the trans-cleavage activity but also disintegrated S2 into fragments, which could form hairpin structures autonomously. Therefore, the CV scanning peak ushered in a significant upward fluctuation once again (curve g).

Simultaneously, the detailed modification process was also demonstrated by the EIS spectra, and the electron transfer resistance (R_{et}) was calculated precisely according to the equivalent circuit (Figure 5B, inset). In the high-frequency field, a regular semicircle of bare paper was observed (curve a). As expected, after 3D-rGO and AuPd NPs were decorated on the paper electrode sequentially, a successive decrease in R_{et} was detected, which proved that the coating and doping of the electrode contributed to improve the conductivity (curves b and c). Immediately, the R_{et} sustained a progressive increase and reached the peak when the g-C_3N_4 NS-DNA duplex probe and MCH were successively immobilized on the as-modified electrode, because of the obstruction of electron transfer by biological macromolecules (curves d and e). After incubation with intermediate DNA, a semicircle with a reduced diameter was detected in the high-frequency region, indicating that S1 on the electrode surface was attracted away and S2 automatically formed a circular hairpin (curve f). Surprisingly, as the thorough incubation of CRISPR/Cas12a/crRNA, S2 was nonspecifically trans-cleaved and the steric hindrance effect on the electrode surface was unprevailing, resulting in a sudden decrease in R_{et} (curve g). Thus, the abovementioned variations in CV and EIS spectra could testify the effective construction of the biosensor.

Performance Analysis of the ECL Biosensor. To accomplish the optimum experimental performance, multifarious improvement measures have been implemented (see the Supporting Information). Furthermore, the performance measurement of the constructed biosensor was performed for the detection of miRNA-141 under the optimum conditions. As displayed in Figure 6A, the ECL intensity was monitored by controlling different concentration gradients of miRNA-141, which exhibited that the higher the concentration of miRNA-141, the more thorough the trans-cleavage activity of CRISPR/Cas12a/crRNA and the weaker the ECL signal. Moreover, there was a linear correlation between the logarithm of miRNA-141 concentration in the range from 1 fM to 10 nM and the ECL intensity (Figure 6B). The regression equation was $I = -1385.455 \lg c_{miRNA} - 9818.250$ ($R^2 = 0.994$), and the detection limit was evaluated to be 0.331 fM at a signal-to-noise ratio (SNR) of 3, which demonstrated the superiorities of the wide monitoring range and low detection limit of the biosensor in this work.

To further assess the specificity and selectivity of the proposed biosensors for detecting of miRNA-141, different interference sequences of RNA with high concentration, such as miRNA-101, miRNA-210, and miRNA-155, were selected to take the place of the target miRNA-141 at the same experimental conditions (Figure 6C). As shown in the results, miRNA-101 (100 nM), miRNA-210 (100 nM), and miRNA-155 (100 nM) revealed no significant difference from the blank sample. After blending miRNA-210 (100 nM), miRNA-101(100 nM), and miRNA-155 (100 nM) with the target miRNA-141 (1 nM), the intensity of ECL plummeted to the minimum for which the proposed biosensor was equipped with outstanding selectivity in the presence of 1 nM miRNA-141 only. Moreover, since stability was an important parameter to diagnose the performance of the biosensor, three successive scans of miRNA-141 with various concentrations were performed and presented by the ECL signal. The results revealed that the proposed biosensor exhibited remarkable stability in the linear range of concentrations (Figure 6D).

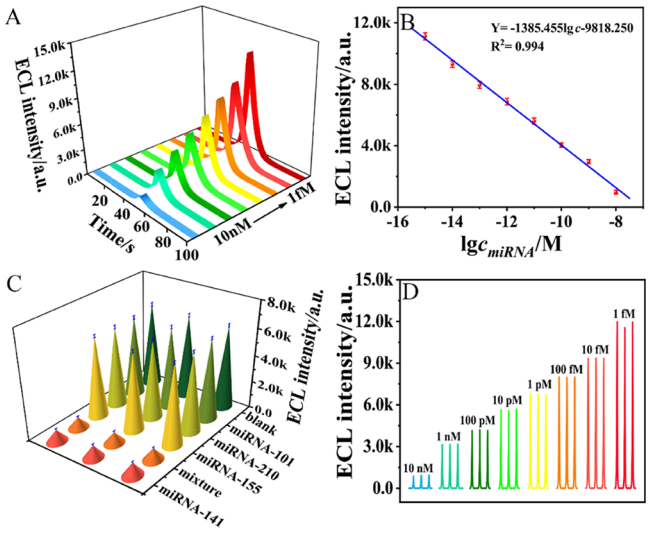

Figure 6. (A) ECL intensity potential lineaments of the proposed biosensor incubated with miRNA-141 concentrations of 1 fM, 10 fM, 100 fM, 1 pM, 10 pM, 100 pM, 1 nM, and 10 nM. (B) Correlation curve for the relationship of the logarithm of the miRNA-141 concentration vs the ECL intensity. (C) Selectivity with various interfering substrates (error bars show S.D., $n = 3$). (D) Stability with different concentrations of miRNA-141 from 1 fM to 10 nM.

The reproducibility of the proposed ECL biosensor was evaluated by intra- and interassay differences (relative standard deviation (RSD)). Herein, standard solutions including three different concentrations of miRNA-141 (10 fM, 10 pM, and 10 nM) were used to evaluate RSD ($n = 3$). As confirmed by the experimental data, the RSD values of intra-assay analysis were 5.6, 4.8, and 4.2% at 10 fM, 10 pM, and 10 nM miRNA-141, respectively, while the RSD values of interassay analysis using different batches of the biosensor were 8.3, 9.1, and 8.6% at 10 fM, 10 pM, and 10 nM miRNA-141, respectively. Therefore, the reproducibility of the proposed biosensor was satisfactory.

CONCLUSIONS

In summary, a high-sensitive ECL sensing platform on the basis of 3D DNA walker-assisted CRISPR/Cas12a trans-cleavage was successfully achieved for the detection of miRNA-141. The high-performance AuPd NP/3D-rGO/PWE not only provided an appropriate environment for enhancing the primeval specific surface area, expanding the conductivity of the electrode, and increasing the loading sites of biomolecules but also could be used as a signal emitter to dramatically improve the cathode emission efficiency of g-C_3N_4 NSs. Furthermore, the 3D DNA walker was designed in this work to realize target recycling amplification, which could initiate the subsequent strand reaction to output massive intermediate products and improve the accuracy of target conversion toward nanoorbitals. In addition, the CRISPR/Cas12a system with high kinetic catalytic efficiency allowed the execution of nonspecific trans-cleavage of the hairpin reporter, which

https://doi.org/10.1021/acs.analchem.1c03183
Anal. Chem. 2021, 93, 13373−13381

further avoided the false-positive and false-negative problems. Therefore, this method achieved a trace detection with low background noises, which prosperously developed the combination of CRISPR/Cas12a and biomolecules and chemical analysis and provided a worthwhile contribution for biochemical research and clinical application.

■ ASSOCIATED CONTENT

Supporting Information

The Supporting Information is available free of charge at https://pubs.acs.org/doi/10.1021/acs.analchem.1c03183.

Reagents and instruments; design and fabrication of the LPD; preparation of Au NP seed solution; PAGE analysis of the 3D DNA walker; optimized conditions of the biosensor; and real samples analysis (PDF)

■ AUTHOR INFORMATION

Corresponding Authors

Chaomin Gao − *School of Chemistry and Chemical Engineering, University of Jinan, Jinan 250022, P.R. China*; Email: chm_gaocm@163.com

Shenguang Ge − *Institute for Advanced Interdisciplinary Research, University of Jinan, Jinan 250022, P.R. China*; orcid.org/0000-0002-0537-6491; Phone: +86-531-82767161; Email: chm_gesg@163.com

Authors

Qian Wang − *Institute for Advanced Interdisciplinary Research and School of Chemistry and Chemical Engineering, University of Jinan, Jinan 250022, P.R. China*

Yaqi Liu − *Institute for Advanced Interdisciplinary Research, University of Jinan, Jinan 250022, P.R. China*

Jixian Yan − *Shandong Provincial Center for Prevention and Control of Solid Waste and Hazardous Chemical Pollution, Jinan 250000, P.R. China*

Yunqing Liu − *Institute for Advanced Interdisciplinary Research, University of Jinan, Jinan 250022, P.R. China*

Jinghua Yu − *School of Chemistry and Chemical Engineering, University of Jinan, Jinan 250022, P.R. China*

Complete contact information is available at: https://pubs.acs.org/10.1021/acs.analchem.1c03183

Author Contributions

#Q.W. and Y.L. contributed equally to this work.

Notes

The authors declare no competing financial interest.

■ ACKNOWLEDGMENTS

This work was supported by the National Natural Science Foundation of China (22074053, 21775055, and 21874055); Excellent Youth Innovation Team in Universities of Shandong (2019KJC016); the Project of "20 items of University" of Jinan (2020GXRC047 and 2018GXRC001); and the Taishan Scholars program and Case-by-Case Project for Top Outstanding Talents of Jinan.

■ REFERENCES

(1) Zhang, S.; Cheng, J.; Shi, W.; Li, K. B.; Han, D. M.; Xu, J. J. *Anal. Chem.* **2020**, *92*, 5952−5959.

(2) Zhang, Y.; Chen, W.; Zhang, Y.; Zhang, X.; Liu, Y.; Ju, H. *Angew. Chem., Int. Ed.* **2020**, *59*, 21454−21459.

(3) Xue, C.; Zhang, S. X.; Ouyang, C. H.; Chang, D.; Salena, B. J.; Li, Y.; Wu, Z. S. *Angew. Chem., Int. Ed.* **2018**, *57*, 9739−9743.

(4) Carrara, S.; Aliprandi, A.; Hogan, C. F.; De Cola, L. *J. Am. Chem. Soc.* **2017**, *139*, 14605−14610.

(5) Cai, W. R.; Zhang, G. Y.; Lu, K. K.; Zeng, H. B.; Cosnier, S.; Zhang, X. J.; Shan, D. *ACS Appl. Mater. Interfaces* **2017**, *9*, 20904−20912.

(6) Babamiri, B.; Bahari, D.; Salimi, A. *Biosens. Bioelectron.* **2019**, *142*, No. 111530.

(7) Alim, S.; Vejayan, J.; Yusoff, M. M.; Kafi, A. K. M. *Biosens. Bioelectron.* **2018**, *121*, 125−136.

(8) Wang, G.; Zannikou, M.; Lofchy, L.; Li, Y.; Gaikwad, H.; Balyasnikova, I. V.; Simberg, D. *ACS Nano* **2021**, *15*, 11880−11890.

(9) Gnaim, S.; Scomparin, A.; Das, S.; Blau, R.; Satchi-Fainaro, R.; Shabat, D. *Angew. Chem., Int. Ed.* **2018**, *57*, 9033−9037.

(10) Sun, D.; Lu, J.; Luo, Z.; Zhang, L.; Liu, P.; Chen, Z. *Biosens. Bioelectron.* **2018**, *120*, 8−14.

(11) Bao, Y.; Jiang, Y.; Xiong, E.; Tian, T.; Zhang, Z.; Lv, J.; Li, Y.; Zhou, X. *ACS Sens.* **2020**, *5*, 1082−1091.

(12) Shah, S.; Wee, J.; Song, T.; Ceze, L.; Strauss, K.; Chen, Y. J.; Reif, J. *J. Am. Chem. Soc.* **2020**, *142*, 9587−9593.

(13) Luo, J. H.; Li, Q.; Chen, S. H.; Yuan, R. *ACS Appl. Mater. Interfaces* **2019**, *11*, 27363−27370.

(14) Škugor, M.; Valero, J.; Murayama, K.; Centola, M.; Asanuma, H.; Famulok, M. *Angew. Chem., Int. Ed.* **2019**, *58*, 6948−6951.

(15) Wang, Y.; Wang, Y.; Liu, S.; Sun, W.; Zhang, M.; Jiang, L.; Li, M.; Yu, J.; Huang, J. *Anal. Chim. Acta* **2021**, *1143*, 21−30.

(16) Wang, Z.; Jia, N.; Zhou, X.; Han, J.; Bu, H. *ACS Appl. Bio Mater.* **2021**, *4*, 3571−3578.

(17) Yin, Y.; Chen, G.; Gong, L.; Ge, K.; Pan, W.; Li, N.; Machuki, J. O.; Yu, Y.; Geng, D.; Dong, H.; Gao, F. *Anal. Chem.* **2020**, *92*, 9247−9256.

(18) Chen, Z.; Wang, C.; Hao, L.; Gao, R.; Li, F.; Liu, S. *Biosens. Bioelectron.* **2019**, *128*, 104−112.

(19) Athreya, N. B. M.; Sarathy, A.; Leburton, J. P. *ACS Sens.* **2018**, *3*, 1032−1039.

(20) Liu, R.; Zhang, S.; Zheng, T. T.; Chen, Y. R.; Wu, J. T.; Wu, Z. S. *ACS Nano* **2020**, *14*, 9572−9584.

(21) Daems, D.; Pfeifer, W.; Rutten, I.; Saccà, B.; Spasic, D.; Lammertyn, J. *ACS Appl. Mater. Interfaces* **2018**, *10*, 23539−23547.

(22) Zhao, L.; Sun, R.; He, P.; Zhang, X. *Anal. Chem.* **2019**, *91*, 14773−14779.

(23) Gao, Q.; Zhao, Y.; Xu, K.; Zhang, C.; Ma, Q.; Qi, L.; Chao, D.; Zheng, T.; Yang, L.; Miao, Y.; Han, D. *Angew. Chem., Int. Ed.* **2020**, *59*, 23564−23568.

(24) Ou, Y.; Jin, X.; Fang, J.; Tian, Y.; Zhou, N. *Microchem. J.* **2020**, *156*, No. 104823.

(25) Dai, Y.; Wu, Y.; Liu, G.; Gooding, J. J. *Angew. Chem., Int. Ed.* **2020**, *132*, 20938−20950.

(26) Zhou, T.; Huang, R.; Huang, M.; Shen, J.; Shan, Y.; Xing, D. *Adv. Sci.* **2020**, *7*, No. 1903661.

(27) Wu, H.; Chen, X.; Zhang, M.; Wang, X.; Chen, Y.; Qian, C.; Wu, J.; Xu, J. *TrAC-Trends Anal. Chem.* **2021**, *135*, No. 116150.

(28) Yin, K.; Ding, X.; Li, Z.; Zhao, H.; Cooper, K.; Liu, C. *Anal. Chem.* **2020**, *92*, 8561−8568.

(29) Xiong, Y.; Zhang, J.; Yang, Z.; Mou, Q.; Ma, Y.; Xiong, Y.; Lu, Y. *J. Am. Chem. Soc.* **2020**, *142*, 207−213.

(30) Kachwala, M. J.; Smith, C. W.; Nandu, N.; Yigit, M. V. *Anal. Chem.* **2021**, *93*, 1934−1938.

(31) Som, M.; Lal, R.; Ruiz-Velasco, V. *Bioconjugate Chem.* **2020**, *31*, 2697−2711.

(32) Wang, G.; Tian, W.; Liu, X.; Ren, W.; Liu, C. *Anal. Chem.* **2020**, *92*, 6702−6708.

(33) Mekler, V.; Kuznedelov, K.; Severinov, K. *J. Biol. Chem.* **2020**, *295*, 6509−6517.

(34) Li, B.; Xia, A.; Zhang, S.; Suo, T.; Ma, Y.; Huang, H.; Zhang, X.; Chen, Y.; Zhou, X. *Biosens. Bioelectron.* **2021**, *173*, No. 112619.

(35) Mukama, O.; Wu, J.; Li, Z.; Liang, Q.; Yi, Z.; Lu, X.; Liu, Y.; Liu, Y.; Hussain, M.; Makafe, G. G.; Liu, J.; Xu, N.; Zeng, L. *Biosens. Bioelectron.* **2020**, *159*, No. 112143.
(36) Li, H.; Li, M.; Yang, Y.; Wang, F.; Wang, F.; Li, C. *Anal. Chem.* **2021**, *93*, 3209−3216.
(37) Fu, X.; Shi, Y.; Peng, F.; Zhou, M.; Yin, Y.; Tan, Y.; Chen, M.; Yin, X.; Ke, G.; Zhang, X. B. *Anal. Chem.* **2021**, *93*, 4967−4974.
(38) Zhang, Y.; Xu, J.; Zhou, S.; Zhu, L.; Lv, X.; Zhang, J.; Zhang, L.; Zhu, P.; Yu, J. *Anal. Chem.* **2020**, *92*, 3874−3881.
(39) Yang, H.; Zhang, Y.; Li, L.; Zhang, L.; Lan, F.; Yu, J. *Anal. Chem.* **2017**, *89*, 7511−7519.
(40) Malola, S.; Häkkinen, H. *J. Am. Chem. Soc.* **2019**, *141*, 6006−6012.
(41) Gao, X.; Li, J.; Luan, M.; Li, Y.; Pan, W.; Li, N.; Tang, B. *Biosens. Bioelectron.* **2020**, *147*, No. 111755.

https://doi.org/10.1021/acs.analchem.1c03183
Anal. Chem. 2021, 93, 13373−13381